

Fine-tuning vision foundation model for crack segmentation in civil infrastructures

K. Ge¹, C. Wang², Y. T. Guo^{1*}, Y. S. Tang¹, Z. Z. Hu¹

¹*Shenzhen International Graduate School, Tsinghua University, Shenzhen, China*

²*Department of Civil Engineering, Tsinghua University, Beijing, China*

Abstract

Large-scale foundation models have become the mainstream deep learning method, while in civil engineering, the scale of AI models is strictly limited. In this work, a vision foundation model is introduced for crack segmentation. Two parameter-efficient fine-tuning methods, adapter and low-rank adaptation, are adopted to fine-tune the foundation model in semantic segmentation: the Segment Anything Model (SAM). The fine-tuned CrackSAM model is much larger than all the existing crack segmentation models but shows excellent performance. To test the zero-shot performance of the proposed method, two unique datasets related to road and exterior wall cracks are collected, annotated and open-sourced, for a total of 810 images. Comparative experiments are conducted with twelve mature semantic segmentation models. On datasets with artificial noise and previously unseen datasets, the performance of CrackSAM far exceeds that of all state-of-the-art models. CrackSAM exhibits remarkable superiority, particularly under challenging conditions such as dim lighting, shadows, road markings, construction joints, and other interference factors. These cross-scenario results demonstrate the outstanding zero-shot capability of foundation models and provide new ideas for developing vision models in civil engineering.

Keywords: Crack segmentation, Parameter-efficient fine-tuning, Vision Transformer, Transfer learning, Zero-shot

* Corresponding author: Y. T. Guo (guoyutao@sz.tsinghua.edu.cn)

Emails: K. Ge (gk22@mails.tsinghua.edu.cn),

1. Introduction

Cracks are common in engineering structures, which may reduce the load-bearing capacity and stiffness of structures and lead to corrosion of internal reinforcements, reducing durability and causing structural failure [1]. Therefore, identifying and analysing cracks are important in structural health monitoring (SHM).

Traditionally, crack detection is carried out manually, which is costly, subjective and inefficient. Emerging SHM methods have paved the way for more automated, efficient and intelligent monitoring. Multiple nondestructive monitoring methods, including contact-based technologies such as sensors [2] and contactless methods such as ultrasound [3] and infrared thermography [4], are widely used in crack analyses. A prominent technology is the use of unmanned aerial vehicles (UAVs). Equipped with devices such as high-resolution cameras, radar, and infrared cameras [5], UAVs have been applied in a series of crack assessment tasks [6][7][8].

The aim of crack segmentation is to classify crack images pixelwise to distinguish between cracks and backgrounds, which entails image processing technologies. More than a decade ago, the main approaches for crack segmentation were filters [9], wavelet transforms [10], and other methods for denoising crack images.

In recent years, deep learning technologies have achieved rapid progress and are widely employed in computer vision (CV) tasks. Therefore, neural networks have become the mainstream approach for crack segmentation problems since 2016 [11]. The models can be divided into two categories from the architectural perspective: CNN-based networks and Transformer-based [12] networks. The former can be seen as a series of stacked local filters, enhancing the model's receptive field through multiscale feature fusion. The latter effectively addresses the challenge of capturing long-distance dependencies through an attention mechanism.

A problem that cannot be ignored still exists: the crack segmentation model trained on a certain dataset may not be generalizable to other datasets. Pretrained models typically contain biases in the training set and tend to overfit on them but will perform poorly on unseen datasets. Chen noted the problem of cross-scenario/scale generalizability of defect detection models, where a pretrained crack segmentation model is not readily generalizable to sophisticated defect types or large-scale images, with the intersection over union (IoU) decreasing from 46.9% to 14.2 and 1.3%, respectively [13].

Crack segmentation is a highly class-imbalanced classification problem and is affected by many interference factors [14], including too-fine cracks, low resolution, different shooting distances, blurring, shadows, occlusions, traffic and pedestrian flows, and different working conditions.

However, the crack images commonly used for training are much cleaner. These factors seriously hinder the deployment of pretrained models for identifying cracks in engineering practice.

Inspired by the excellent generalization and zero-shot performance of large-scale foundation models, in this paper, parameter-efficient fine-tuning (PEFT) technologies are applied to introduce the vision foundation model SAM into crack segmentation. Two datasets with severe interference under different working conditions are collected. Evaluation of the proposed CrackSAM is focused on the inference performance on datasets with artificial noise and zero-shot performance on previously unseen datasets. Relatively few studies have evaluated the zero-shot capability of pretrained crack segmentation models on different datasets. However, this is precisely the most concerning engineering aspect. Without this, models will remain at the research stage and cannot be practically implemented. To the best of the authors' knowledge, this is the first work to fine-tune a large vision foundation model for crack segmentation.

The contributions of this paper are summarized as follows:

- A road crack dataset and an exterior wall crack dataset are collected using mobile phones and UAVs.
- Two PEFT methods, adapter [15] and low-rank adaptation (LoRA) [16], are employed to apply SAM for crack segmentation.
- Compared with twelve state-of-the-art (SOTA) models, the fine-tuned CrackSAM exhibits outstanding performance on datasets with artificial noise and on previously unseen datasets. Excellent zero-shot identification of cracks is achieved without any additional training.
- The collected and labelled datasets, models, and pretrained weights will be publicly available after acceptance.

The remainder of this paper is arranged as follows. Section 2 reviews the relevant related studies. Section 3 describes the preparation of the datasets. Section 4 introduces the model architecture and fine-tuning methods. Section 5 presents the ablation studies and experimental results. Section 6 compares the proposed method with twelve other SOTA methods.

2. Relevant work

2.1 Models for crack segmentation

Semantic segmentation tasks emphasize global context information. Consequently, for CNN-based crack segmentation architectures, the UNet architecture [17] with skip connections and pyramid architecture fused with multiscale feature maps, such as FPN [18], PSPNet [19], and DeepLabV3+ [20], have achieved excellent performance in various crack segmentation tasks. Zhang et al. [21] used

an improved UNet architecture to integrate high-level features and shallow crack features. Ren et al. [22] employed methods such as dilated convolutions, spatial pyramid pooling, and skip connections, to achieve feature aggregation and resolution reconstruction in crack segmentation. Dais et al. [23] combined UNet and FPN and integrated multiple backbones, such as VGG, ResNet, and MobileNet, to conduct comparative experiments on crack segmentation for masonry structures.

Due to the dominance of the Transformer architecture in recent years in CV tasks, Vision Transformer (ViT) [24], Swin Transformer [25], SegFormer [26] and many Transformer-based architectures have been widely used in crack segmentation tasks. Shamsabadi et al. [27] used a TransUNet model with a hybrid CNN-ViT backbone to segment cracks in a dataset with very little semantic information. The performance of the proposed method was superior to that of CNN-based UNet and DeepLabV3+ while also exhibiting greater noise robustness. Guo et al. [28] employed an encoder-decoder architecture with a Swin Transformer backbone, achieving superior segmentation results on road surface cracks compared to models with UNet and ResNet as backbones.

However, small models trained on limited datasets still face issues of insufficient recognition capabilities and poor generalizability.

2.2 Vision foundation models

Foundation models can be regarded as a new general paradigm of AI and have stronger intelligence than traditional models. These methods are usually based on Transformer architectures with billions of parameters. The realization of the foundation model entails large-scale pretraining on large datasets using massive GPUs [29]. In CV, SAM [30] is a recently proposed foundation model for semantic segmentation, which is trained on more than 1 billion masks from 11 million images. Large-scale pretraining endows SAM with the ability to respond to various downstream tasks in a zero-shot manner. SegGPT [31] is also a similar model that is capable of segmenting everything in context with one single model. SEEM [32] achieves semantic, instance, and panoptic segmentation through diverse prompts such as textual, visual, and referring region prompts. DINOv2 [33] is a vision foundation model trained in a self-supervised manner. The model learns directly from images without the need for text guidance. Its backbone can be employed in various downstream tasks, such as image classification, instance recognition, semantic segmentation, and depth estimation.

However, directly applying vision foundation models for crack segmentation is not feasible. Ahmadi et al. [34] utilized SAM for crack segmentation and found that SAM did not perform well for spalled cracks. Moreover, the masks of cracks cannot be directly obtained, as shown in Figure 1. Consequently, it is necessary to fine-tune the SAM to learn the specific semantics of cracks.



Figure 1 Example image of direct application of the SAM for crack segmentation.

2.3 Transfer learning and zero-shot learning

Transfer learning is a technique that involves leveraging knowledge learned from one task or domain to improve the performance of another related task or domain. It involves transferring the learned representations, features, and patterns acquired during the training process of a source task to a target task with limited labelled data.

Transfer learning has been widely practised in crack segmentation tasks. Zhou et al. [35] utilized the pretrained weights from Imagenet-1k [36] to initialize the weights of the backbone to solve the data dependency of the Swin Transformer. The parameters of the backbone are frozen for the first 50 epochs and unfrozen for the latter 50 epochs. Lau et al. [37] compared such a "two-stage" training strategy with a standard training procedure and found that UNet trained with the former method had a better effect. Gao et al. [38] established a hierarchical transfer learning architecture in which the pretrained model for localization and segmentation tasks directly inherited the well-trained backbone used for classification tasks.

Zero-shot learning is a subfield of transfer learning, which is used to classify test instances as an unseen class [39]. In crack segmentation tasks, there may be confusing interference from previously unseen objects in practical engineering situations, and the pretrained model needs to successfully classify this type of semantic information. Therefore, in this work, zero-shot learning can be evidenced by the ability to identify cracks in complex working conditions beyond the training set.

In AI-aided SHM, traditional transfer learning methods can be summarized as initializing the backbone of the model with high-quality pretrained weights (Figure 2(a)). During training, it is common in some studies to fine-tune only downstream networks (Figure 2(b)) or to freeze certain layers initially and then unfreeze and train all layers together. This full fine-tuning process requires significant GPU memory usage and sufficient data support.

Nevertheless, the scarcity of high-quality annotated datasets and limited computational resources make full fine-tuning of a foundation model in civil engineering impossible. For this reason, PEFT methods must be adopted.

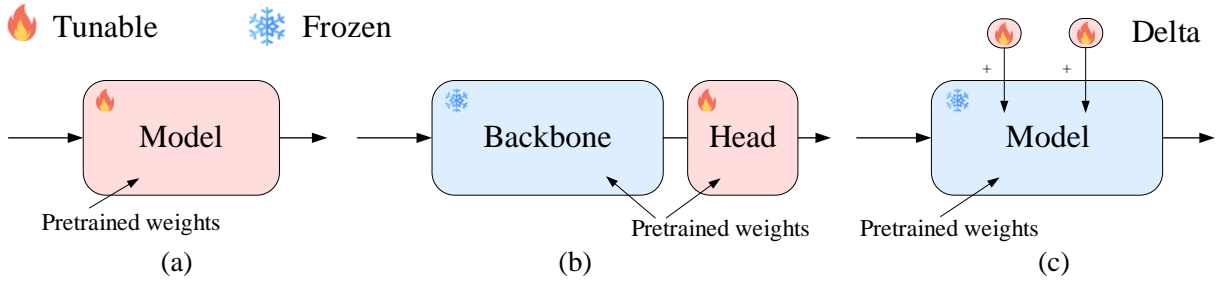


Figure 2 Fine-tuning methods for pretrained models. (a) Full fine-tuning. (b) Fine-tuning of downstream networks. (c) PEFT.

2.4 PEFT

The PEFT is a lighter but more efficient fine-tuning method that is specifically designed for Transformer architectures. With fewer resources and training iterations, PEFT can preserve the original knowledge of pretrained foundation models and avoid catastrophic forgetting.

By introducing a few trainable parameters (less than 5%) that do not exist in the original network, the pretrained foundation model can be adapted for downstream tasks. Compared to other methods that train some or all the layers, PEFT essentially involves "delta-tuning" [40], as shown in Figure 2(c). For example, prefix-tuning achieves comparable performance in the full data setting by adding a trainable "soft prompt" to all the key and value matrices in Transformer layers [41] and even outperforms full fine-tuning in low data settings. Prompt-tuning, as a simpler version of prefix-tuning, adds only soft prompts to the input embeddings [42].

The PEEF of the SAM has already been applied to medical segmentation fields. Chen et al. [43] proposed the SAM-Adapter, which is effective in camouflaged object detection, shadow detection, and polyp segmentation. Wu et al. [44] also fine-tuned SAM with an adapter-based strategy on 19 medical image segmentation tasks, including CT, MRI, ultrasound images, fundus images, and dermoscopic images. Zhang et al. [45] applied the LoRA-based strategy to fine-tune the SAM for multiorgan segmentation in the Synapse dataset, which is on par with the SOTA method.

However, similar methods have not yet been applied in crack segmentation tasks. The most widely utilized PEFT technologies, adapter and LoRA, will be utilized in this work.

3. Data preparation

3.1 Dataset for pretraining

The large labelled crack segmentation dataset collected by Khanhha [46] is utilized in this study. The Khanhha dataset is a union of multiple open-source subdataset, including CRACK500 [47], GAPs384 [48], CFD [49], AEL [50], CrackTree200 [51], CrackForest [49], and DeepCrack [52].

There are 9,603 images for training and 1,695 images for testing, with a resolution of 448×448. The dataset comes from various sources, including road surfaces, pavements, walls, and bridges. The richness of sources allows the model trained on this dataset to perceive cracks of different working conditions and scales, thus leading to a certain degree of generalization. However, inconsistent annotation thicknesses in different datasets can have a certain negative impact on the model.

The annotation of the subdataset CrackTree200 is too fine compared to that of the other datasets, with the width of the crack masks being only one pixel. This inconsistent labelling strategy made it difficult for previous studies [53][54] to identify cracks in the CrackTree200 dataset; therefore, this dataset was manually relabelled by experts. The relabelled CrackTree200 dataset will also be available together with the following collected datasets.

3.2 Datasets collected for zero-shot

Two unique crack datasets are captured for evaluating the model's zero-shot performance: Road420 and Facade390. The pixel-level binary masks of all the collected datasets are obtained via expert annotation. All the images and masks taken were converted into RGB and grayscale images and downsampled to a size of 448×448.

3.2.1 Road420

The Road420 consists of 420 images of asphalt concrete and cement concrete road surfaces with cracks. The pictures contain considerable interfering information, such as shadows, occlusions, road signs, vehicles, manhole covers, people, and leaves. Some small cracks are difficult for the naked eye to recognize after downsampling. Some of the images were taken at night. The image semantics of some interfering factors have never appeared in the Khanhha dataset, and the deliberate introduction of such interference makes zero-shot learning very challenging on this dataset. All the images were captured with an iPhone 14 Pro. Representative sample images are shown in [Figure 3](#).



Figure 3 Sample images of Road420.

3.2.2 Facade390

The Facade390 is composed of cracks on the exterior walls and columns of buildings captured

by UAV. Because the UAV must maintain a safe distance from the building during operation and may experience displacement during hovering, the captured images may be blurry, and some fine cracks may not be clearly visible. The identification of these cracks is susceptible to interference from various factors, such as wall stains, peeling, water traces, shadows, paint, vegetation, construction joints, and other extraneous factors. The cracks in Facade390 are generally not structural cracks but may introduce unsettling risks such as water seepage. The UAV employed in this study was a Dajiang Mini 3. Some representative sample images are presented in [Figure 4](#).



Figure 4 Sample images of Facade390.

3.2.3 Concrete3k

Concrete3k is a large, ready-made dataset with 3,000 image-label pairs of concrete cracks contributed by [\[53\]\[55\]](#), it will also be leveraged for zero-shot images.

4. Methodology

4.1 Overall architecture

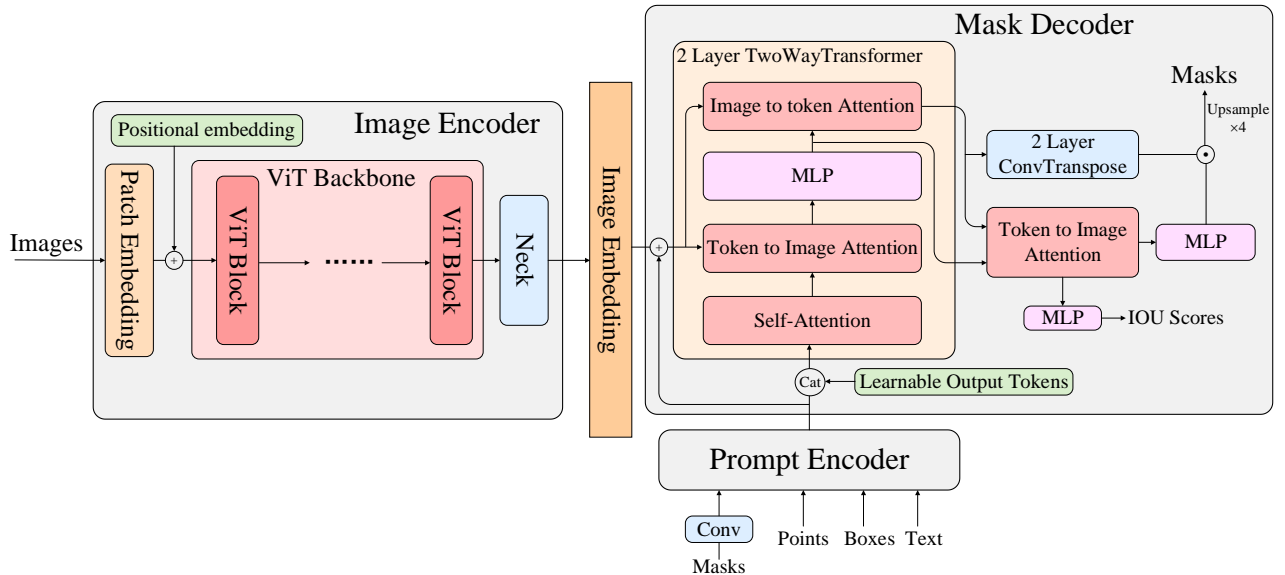


Figure 5 The original overall architecture of the SAM.

The SAM is composed of three key components: an image encoder, a prompt encoder and a mask decoder, as shown in [Figure 5](#). The latter two parts are much lighter than the image encoder.

4.1.1 ViT block

The ViT block is composed of two parts: window attention and a multilayer perceptron (MLP), as shown in [Figure 6](#).

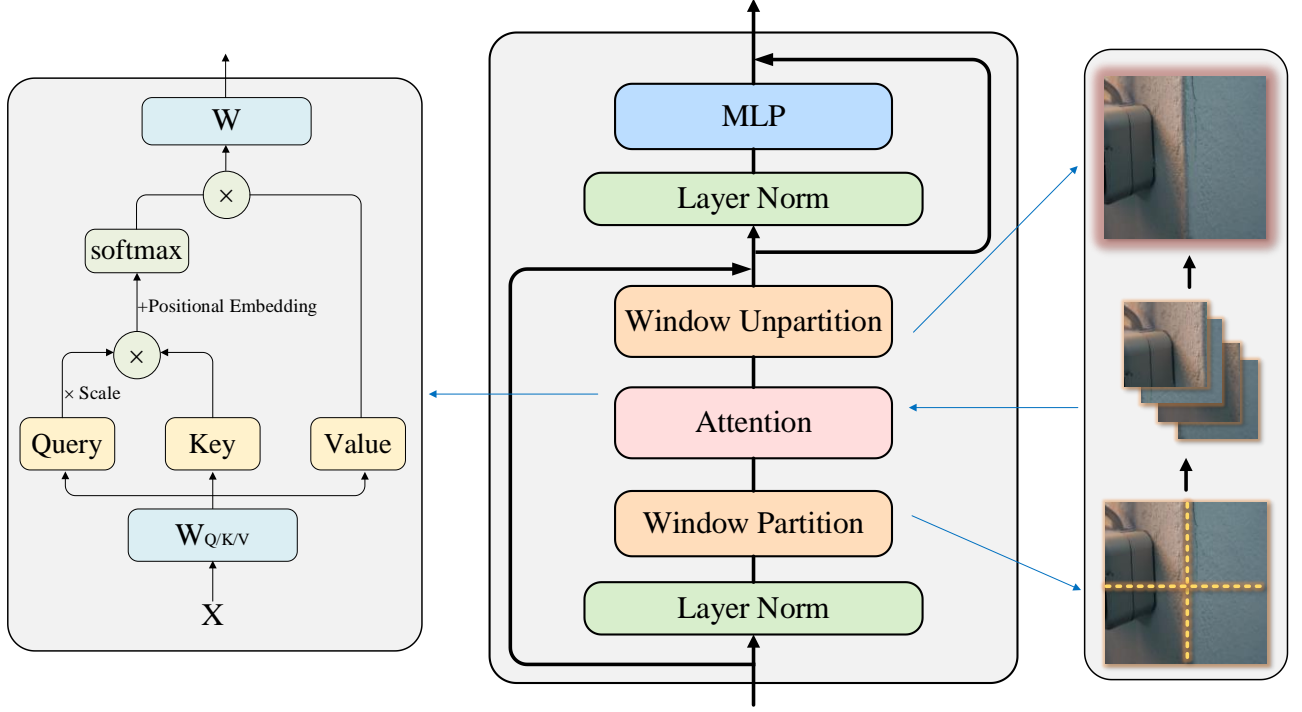


Figure 6 The architecture of the ViT block.

First, the input patches $x_p \in \mathbb{R}^{H \times W \times C}$ undergo a window partition with a size of w and are separated into N nonoverlapping windows $x \in \mathbb{R}^{N \times w \times w \times C}$, where $N=HW/w^2$. The window size is set to 14 here. Then, a multihead self-attention approach is applied to x .

x is divided along the channel dimension and feed into multiple attention heads. In the i -th head, query vector Q and key-value pairs K and V are obtained via a learnable linear layer:

$$Q_i / K_i / V_i = W_{Q_i / K_i / V_i} x_i + b_{Q_i / K_i / V_i} \quad (1)$$

Dot production is computed to calculate the similarity scores between Q and K , which are divided by the square root of the dimension size K for scaling. The result is normalized by a softmax activation function after a learnable positional embedding is added to it. The resulting attention weights are multiplied by V to obtain the output for each head:

$$Atten_i = softmax\left(\frac{Q_i K_i^T}{\sqrt{d_k}} + pos\right) V_i \quad (2)$$

The outputs of each head are concatenated, and feed into a linear layer. Finally, the windows are reorganized into their original shapes $x_o \in \mathbb{R}^{H \times W \times C}$.

The MLP is a fully connected neural network stacked in multiple layers that expands the original dimensions fourfold and compresses it back with Gaussian error linear unit (GELU) activation [56].

The window attention and the MLP inputs are normalized through layer normalization [57]. Moreover, residual connections [58] are added to each module.

4.1.2 Image encoder

The image encoder is an MAE [59] pretrained ViT and consists of a patch embedding layer, a learnable positional embedding, a ViT backbone and a neck. The patch embedding layer is a 16×16 convolution with a stride of 16. The absolute positional embedding is added to each position of the feature map. The backbone is a stack of ViT blocks. Based on the size of the backbone, there are three options: ViT-H, ViT-L, and ViT-B. The embedding dimension, number of blocks and number of attention heads for ViT-B are 768, 12 and 12, respectively. For ViT-L, it is 1024, 24 and 16. For ViT-H, it is 1280, 32 and 16. In the neck, the image embedding is fed to a pointwise convolution and a 3×3 convolution to reduce the dimension to 256. Each convolution is followed by layer normalization.

The output of the image encoder is a $16 \times$ downscaled image embedding with 256 dimensions.

4.1.3 Prompt encoder

The prompt encoder receives sparse or dense prompts. However, in this task, the segmentation object (crack) is determined, so the input of the prompt is simplified to none. The default embedding is a learnable vector that is added to each position of the image embedding.

4.1.4 Mask decoder

A set of learnable tokens is concatenated with the prompt embeddings. The obtained tokens, the image embedding, and its positional embedding, are fed into a 2-layer two-way Transformer.

For additional details about the two-way Transformer, refer to the original code. Within the two-way Transformer, the following steps are performed: first, self-attention is conducted on the input tokens; second, cross-attention is applied from the tokens to the image embedding, where the tokens are regarded as queries and the image embedding is treated as keys and values; then, the tokens are updated through an MLP; and finally, an image-to-token cross-attention is carried out. After each attention and MLP layer, a residual connection and a layer normalization are added.

A two-layer transposed convolution with a stride of 2 and a kernel size of 2×2 upsamples the $1/16$ -size image embedding to $1/4$ -size. GELU activation is performed after convolution, and layer normalization is added between the layers.

Tokens are updated through the final cross-attention layer and a 3-layer MLP. The output is a

linear classifier with a shape of $(\text{num_class}, 32)$. The shape of the image embedding is $(32, H/4, W/4)$. Finally, the low-resolution masks with a shape of $(\text{num_class}, H/4, W/4)$ are obtained by a pointwise product. High-resolution masks can be derived through bilinear interpolation of low-resolution masks.

Because the main parameters are concentrated in the ViT blocks, PEFTs are conducted on these blocks. The lightweight prompt encoder and mask decoder are also fine-tuned together [45].

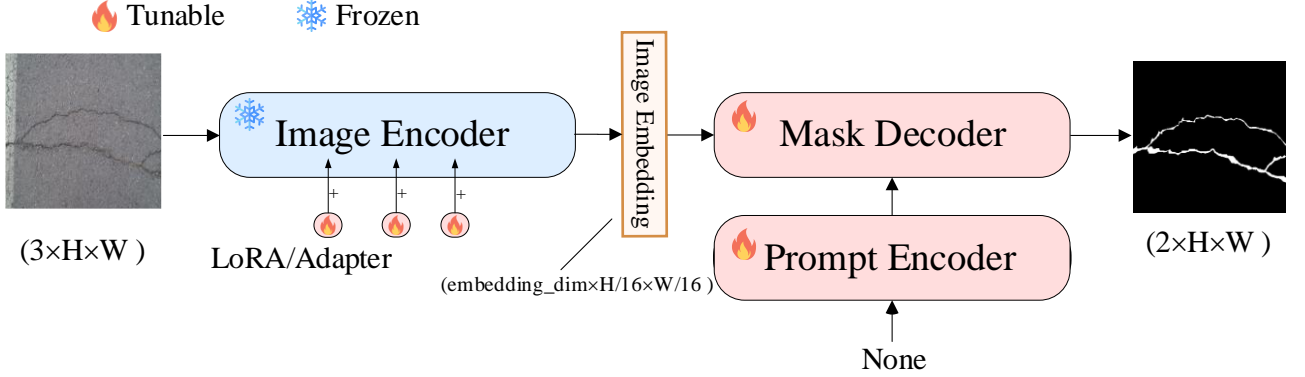


Figure 7 Architecture of the proposed CrackSAM.

The general architecture of the fine-tuned SAM, CrackSAM, is illustrated in Figure 7. Note that the bilinear interpolation of low-resolution masks is performed before feeding them into the final classifier in this architecture to obtain more accurate masks of cracks. This change will also be made to other comparative models in subsequent sections.

4.2 Adapter

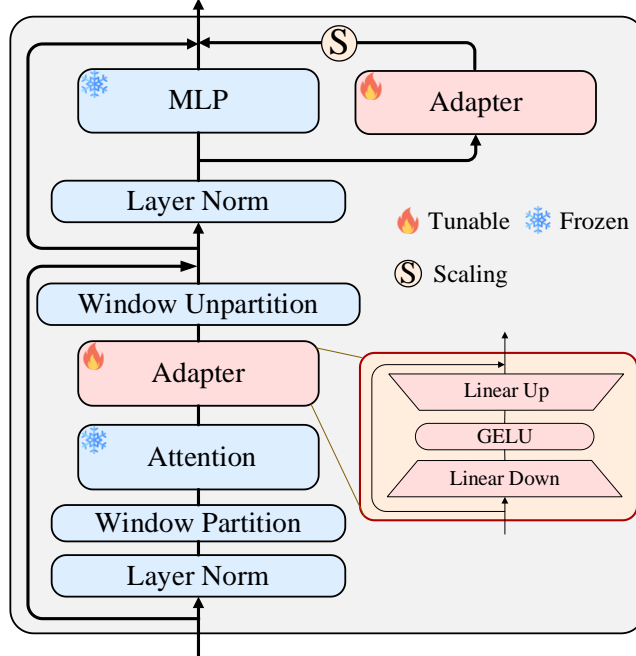


Figure 8 Fine-tuning strategy for the adapter.

The simple design of an adapter makes this approach the most commonly used method in the

field of PEFTs. There are many variants of adapters, which can be either sequential or parallel. In this work, an adapter is sequentially inserted behind the attention layer and parallelly inserted at the MLP [44], as shown in Figure 8. The GELU activation function is employed in the middle, as it provides smoother gradients than does rectified linear unit (ReLU).

An adapter can be regarded as a smaller MLP designed with a bottleneck structure to reduce the parameter count. Initially, the adapter employs a downprojection linear layer with parameters $W_{down} \in \mathbb{R}^{d \times m}$ to project the original d -dimensional features to a smaller dimension m . Subsequently, a nonlinear activation function is applied, followed by an upprojection layer with parameters $W_{up} \in \mathbb{R}^{m \times d}$ to restore the features to the d -dimensional space. Notably, a residual connection is incorporated in this process. The middle dimension m is constrained such that $m \ll d$. Denoting the input as x and the output after adaptation as x' , the transformation is formally expressed as Eq. (3).

$$x' = (W_{up} \cdot \text{GELU}(W_{down}x + b_{down}) + b_{up}) + x \quad (3)$$

For a parallel adapter, there is no need for an additional residual connection, but a scaling factor s is needed to control the extent of the update of the adapter. Given an input x_m for the MLP and its adapted output x'_m , the formula is as follows in Eq. (4).

$$x'_m = s \cdot (W_{up} \cdot \text{GELU}(W_{down} \cdot \text{LN}(x_m) + b_{down}) + b_{up}) + \text{MLP}(\text{LN}(x_m)) + x_m \quad (4)$$

During fine-tuning, the weights of the attention layer and MLP are frozen, and only the weights of the adapter are trained. When the middle dimension is a multiple of the input dimension, the fine-tuning adapter at this point is equivalent to fine-tuning the newly added MLP.

4.3 Low-rank adaptation

LoRA is a reparameterization method that converts the original parameters in a neural network into a parameter-efficient form [40]. A neural network usually consists of many full-rank matrix operations. When migrating to downstream tasks, LoRA assumes that the pretrained model has a small intrinsic rank, and the updating of weights can be achieved on this small subspace.

For a pretrained weight matrix $W_o \in \mathbb{R}^{d \times k}$, a bypass $\Delta W \in \mathbb{R}^{d \times k}$ is added to constrain the update of its weight, and ΔW is decomposed into the product of matrices $A \in \mathbb{R}^{d \times r}$ and $B \in \mathbb{R}^{r \times k}$ using low-rank decomposition, with the rank $r \ll \min(d, k)$. As Figure 9 shows, for the original path $y = W_o x$, the updated result y' is:

$$y' = (W_o + \Delta W)x = W_o x + ABx \quad (5)$$

During fine-tuning, the weight matrix W_o is kept frozen, and only matrices A and B are fine-tuned.

Matrix A is initialized using random Gaussian initialization, and matrix B is initialized to 0 [16].

As a more general approach, LoRA can theoretically be added to any set of weights. In this way, fine-tuning the LoRA is equivalent to full fine-tuning. From a parameter-efficient perspective, LoRA is always added to the attention weights, typically on the query and value components. Due to the adoption of low-rank decomposition, LoRA has fewer parameters than does the adapter. Additionally, the parallel design of LoRA can reduce the inference latency caused by sequential adapter execution.

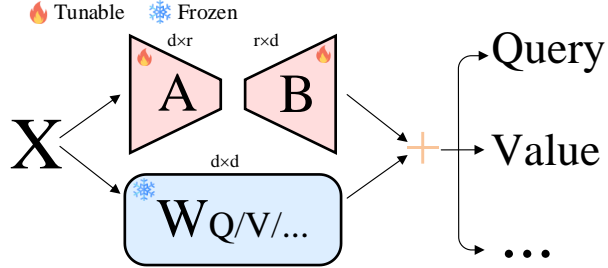


Figure 9 Fine-tuning strategy for the LoRA.

5. Experiment and results

5.1 Implementation details

The primary loss function for semantic segmentation is cross-entropy (Eq. (6)). However, due to the highly imbalanced nature of crack segmentation, the cross-entropy loss tends to rapidly converge to zero during training, thereby allowing the background to dominate the loss [35]. Hence, a more effective approach involves using a weighted combination of cross-entropy and Dice loss (Eq. (7)), as demonstrated in Eq. (8).

$$L_{CE} = -y \log(\hat{y}) - (1-y) \log(1-\hat{y}) \quad (6)$$

$$L_{Dice} = 1 - \frac{2|X \cap Y|}{|X| + |Y|} \quad (7)$$

$$L = \lambda L_{CE} + (1-\lambda) L_{Dice} \quad (8)$$

In Eq. (6), y represents the ground truth labels, taking values of 0 or 1. \hat{y} denotes the probability of the predicted labels. In Eq. (7), X corresponds to the mask regions of the true labels, and Y represents the mask regions of the predicted labels. The parameter λ in Eq. (8) serves as a weighting coefficient and is set to 0.2 in the context of this study.

The learning rate is adjusted using a "poly" policy incorporating a warm-up strategy. Initially, for the first 300 iterations, the learning rate linearly increases from 0 to the initial learning rate of 0.0004. Subsequently, throughout the iterations, the learning rate is dynamically scaled by

multiplying by $(1 - \frac{iter - warm_up}{max_iter})^{power}$, where the power is set to 6. The maximum iteration limit

is set to 140 epochs, with a batch size of 8. The model optimization utilizes AdamW, with parameters β_1 , β_2 , and weight_decay set to 0.9, 0.999, and 0.01, respectively.

A threshold of 0.5 is chosen for mask binarization. Due to the relative abundance of the training dataset, only basic data augmentation techniques, including random rotation and random flipping, are employed. The training process is accelerated using automixed-precision and TensorFloat-32 [45]. Pretrained weights of the SAM are loaded and frozen before training. The best-performing checkpoints for the delta and head in the validation set are saved and selected for subsequent testing. At the inference stage, the final predicted mask is obtained by returning the index of the maximum value in the channel dimension of the masks. The model is established on the PyTorch framework and trained on only one 24 GB RTX3090 GPU.

5.2 Evaluation metrics

The precision (Pr), recall (Re), F1-score (F1), and IoU are employed to evaluate the segmentation performance of the model, as defined in Eq. (9) - Eq. (12).

$$Pr = \frac{TP}{TP + FP} \quad (9)$$

$$Re = \frac{TP}{TP + FN} \quad (10)$$

$$F1 = \frac{2 \cdot Pr \cdot Re}{Pr + Re} \quad (11)$$

$$IoU = \frac{TP}{TP + FP + FN} \quad (12)$$

where true positive (TP) denotes pixels representing cracks that are correctly classified, false positive (FP) represents background pixels erroneously classified as cracks, and false negative (FN) indicates crack pixels misclassified as background.

5.3 Ablation study

In this section, an ablation study is conducted on the parameter setting of the proposed architecture. For the adapter, it is necessary to study the size of the middle dimension and scaling factor. For the LoRA, the positions where the LoRA is applied and the size of the rank should be investigated. The settings of these hyperparameters vary greatly for different downstream tasks. In addition, the impacts of the size of the backbone and the combination of two fine-tuning methods are

studied.

The following experiment discusses the Pr, Re, F1, and IoU metrics (Eq. (9) - Eq. (12)) when a well-trained crack segmentation model is inferring on the test set. Moreover, the model's generalization ability is evaluated by directly applying the pretrained model to three new datasets (Road420, Facade390, and Concrete3k) in a zero-shot manner without any additional training and measuring the IoU metric.

5.3.1 CrackSAM_adapter

As Table 1 shows, introducing a few parameters is sufficient to achieve excellent transfer to downstream tasks. Even when the middle dimension is set to 1, the model can still achieve decent precision. Interestingly, increasing the middle dimension continuously improved the metrics on the test set, but blindly increasing the number of parameters leads to a decrease in generalizability. When the middle dimension is 32, the IoU on the test set decreases by only 0.3% compared to when the middle dimension is 64. However, there are improvements of 1.9%, 3.7%, and 4.8% when performing zero-shot learning on Road420, Facade390, and Concrete3k, respectively. Considering that the number of parameters in the adapter is directly proportional to the middle dimension, setting the middle dimension to 32 is more appropriate.

Table 1 Ablation study on the middle dimension of the adapter.

| Middle dimension | Metric of inference on test set | | | | IoU of zero-shot on the new dataset | | |
|------------------|---------------------------------|--------|--------|--------|-------------------------------------|-----------|------------|
| | Pr | Re | F1 | IoU | Road420 | Facade390 | Concrete3k |
| dim=1 | 0.7554 | 0.7786 | 0.7515 | 0.6270 | 0.5310 | 0.4618 | 0.6743 |
| dim=16 | 0.7664 | 0.7968 | 0.7696 | 0.6479 | 0.6139 | 0.4772 | 0.6461 |
| dim=32 | 0.7676 | 0.7965 | 0.7704 | 0.6495 | 0.6149 | 0.4718 | 0.6718 |
| dim=64 | 0.7674 | 0.8002 | 0.7719 | 0.6513 | 0.6033 | 0.4548 | 0.6412 |

Note that the model's IoU on the Facade390 dataset is relatively low. This is because Facade390 is composed mainly of cracks in building exterior wall materials, which are very fine compared to road cracks. The masks in the training set are mostly coarse segment-wise annotations, such as the masks in the CRACK500 subset. Fine annotations are less prevalent in the training set, resulting in a lower IoU during the zero-shot operation on Facade390. In fact, a well-tuned CrackSAM model can accurately detect the majority of cracks in Facade390 ($Re > 0.9$). Given this, in ablation experiments, priority is given to evaluating the generalization ability of the proposed method based on the Road420 and Concrete3k datasets.

The scaling factor s is introduced to balance the task-agnostic features generated by the frozen backbone and the task-specific features generated by the tunable parallel adapters. As shown in Table 2, setting the scaling factor to 0.2 can yield better performance in terms of generalization.

Table 2 Ablation study on the scaling factor of the adapter.

| Scaling factor | Metric of inference on test set | | | | IoU of zero-shot on new dataset | | |
|----------------|---------------------------------|--------|--------|--------|---------------------------------|-----------|------------|
| | Pr | Re | F1 | IoU | Road420 | Facade390 | Concrete3k |
| $s=0.1$ | 0.7671 | 0.7953 | 0.7693 | 0.648 | 0.6042 | 0.4487 | 0.6597 |
| $s=0.2$ | 0.7676 | 0.7965 | 0.7704 | 0.6495 | 0.6149 | 0.4718 | 0.6718 |
| $s=0.5$ | 0.7716 | 0.7934 | 0.7706 | 0.6499 | 0.609 | 0.4354 | 0.6635 |
| $s=1$ | 0.7702 | 0.7958 | 0.7709 | 0.6500 | 0.6006 | 0.4313 | 0.6426 |
| $s=2$ | 0.7751 | 0.7902 | 0.7707 | 0.6494 | 0.5981 | 0.4586 | 0.6548 |

5.3.2 CrackSAM_LoRA

Table 3 Ablation study on the rank of the LoRA.

| Rank | Metric of inference on test set | | | | IoU of zero-shot on new dataset | | |
|--------|---------------------------------|--------|--------|--------|---------------------------------|-----------|------------|
| | Pr | Re | F1 | IoU | Road420 | Facade390 | Concrete3k |
| $r=1$ | 0.7509 | 0.7941 | 0.7585 | 0.6352 | 0.6176 | 0.4494 | 0.6516 |
| $r=4$ | 0.7620 | 0.7918 | 0.7639 | 0.6416 | 0.6222 | 0.4544 | 0.6798 |
| $r=8$ | 0.7656 | 0.7925 | 0.7665 | 0.6448 | 0.6201 | 0.4601 | 0.6800 |
| $r=16$ | 0.7657 | 0.7947 | 0.7687 | 0.6473 | 0.6200 | 0.4573 | 0.6727 |

According to Table 3, similar to an adapter, fine-tuning a LoRA with a rank set to 1 is quite effective, and at this point, the parameters of the LoRA component are only 0.16 M. As the rank increases, the metrics on the test set continuously improve. The model's generalization reaches saturation when the rank is set to 4 or 8, while it decreases slightly when the rank is set to 16. The decrease in generalization caused by over-parameterization for the LoRA is similar to that for the adapter. Considering the performance and cost, a rank of 4 or 8 is more reasonable.

The LoRA layer can be applied to the query, key, value, and output matrices in the attention layer. As shown in Table 3 and Table 4, when the rank is 8 and the LoRA layer is applied to only the query, even though the number of parameters is equivalent to the situation when the rank is 4 and the LoRA is applied to both the query and value, the latter achieves higher metrics. This finding implies that the position of the LoRA layer is a crucial factor.

Applying LoRA to all four matrices has a similar effect on excessively increasing the rank, resulting in a slight improvement in the metrics of the test set but a decrease in the zero-shot capability. Therefore, it suffices to add LoRA to the query and value matrices alone.

Table 4 Ablation study on the weight type of the LoRA.

| Weight type | Metric of inference on test set | | | | IoU of zero-shot on the new dataset | | |
|----------------------|---------------------------------|--------|--------|--------|-------------------------------------|-----------|------------|
| | Pr | Re | F1 | IoU | Road420 | Facade390 | Concrete3k |
| W_q | 0.7489 | 0.7964 | 0.7575 | 0.6344 | 0.5800 | 0.5122 | 0.6562 |
| W_q, W_v | 0.7656 | 0.7925 | 0.7665 | 0.6448 | 0.6201 | 0.4601 | 0.6800 |
| W_q, W_k, W_v, W_o | 0.7717 | 0.7887 | 0.7690 | 0.6476 | 0.6183 | 0.4602 | 0.6501 |

When comparing adapter and LoRA, the former demonstrates slightly higher metrics on the test set, while the latter exhibits better generalization performance. Considering that LoRA has fewer

parameters than does the adapter, it is recommended to apply CrackSAM_LoRA in engineering.

5.3.3 Combine two PEFT methods or use neither

Here, comparisons are made between simultaneously using both PEFT methods and not using both methods, i.e., employing only the traditional fine-tuning of the head (Figure 2(b)).

Three different parameter scales of the adapter and LoRA combinations are tested. According to Table 5, the effectiveness of combinations of PEFTs depends on the parameter scale. When both the adapter with a middle dimension of 32 and LoRA with a rank of 8 are added simultaneously to the model, compared to the model with only the LoRA of rank 8, as shown in Table 4, the metrics improve slightly. However, considering the obvious increase in the computational cost, there is no significant advantage to combine multiple PEFT methods.

When fine-tuning only the prompt encoder and mask decoder, the performance significantly decreases. The IoU metrics in Table 4 on the test set and three new datasets increase by approximately 15.9%, 28.5%, 7.3%, and 12.2%, respectively, compared to the method of fine-tuning only the head in Table 5. This clearly demonstrates the superiority of the PEFT algorithm over traditional fine-tuning methods because completely freezing the backbone makes it more challenging for the model to extract semantic information related to cracks.

Table 5 Experimental results of combining two methods and using neither method.

| Delta type | Metric of inference on test set | | | | IoU of zero-shot on the new dataset | | |
|---|---------------------------------|--------|--------|--------|-------------------------------------|-----------|------------|
| | Pr | Re | F1 | IoU | Road420 | Facade390 | Concrete3k |
| No PEFT, fine-tune only head | 0.6951 | 0.7188 | 0.6843 | 0.5564 | 0.4826 | 0.4288 | 0.6059 |
| adapter($s^*=0.2$, $dim^*=8$) + LoRA($qv^*, r^*=2$) | 0.7596 | 0.7959 | 0.7657 | 0.6438 | 0.6132 | 0.4560 | 0.6628 |
| adapter($s=0.2$, $dim=16$) + LoRA($qv, r=4$) | 0.7637 | 0.8005 | 0.7703 | 0.6488 | 0.6188 | 0.4639 | 0.6798 |
| adapter($s=0.2$, $dim=32$) + LoRA($qv, r=8$) | 0.7664 | 0.7959 | 0.7696 | 0.6485 | 0.6230 | 0.4862 | 0.6835 |

Note: 1s = scaling factor; 2dim = middle dimension; 3qv = apply LoRA to query and value matrices; 4r = rank.

5.3.4 Backbone size

According to Table 6, the size of the backbone has a significant impact on the fine-tuned model. In general, the larger the backbone is, the more powerful the segmentation ability after fine-tuning. Progressing from ViT-B to ViT-L and then to ViT-H, the segmentation performance and generalization ability improved both for the adapter and the LoRA. This observation aligns with the scaling law of large language models. This difference may be attributed to the richer features extracted by the stronger backbone and the smaller intrinsic dimension. With the same parameter configuration, fine-tuning becomes more effective for large-scale backbones. Therefore, in other experiments, this paper regards only ViT-H as the backbone for CrackSAM.

Table 6 Ablation study on the size of the backbone.

| Delta type | Backbone | Metric of inference on test set | | | | IoU of zero-shot on the new dataset | | |
|------------|----------|---------------------------------|--------|--------|--------|-------------------------------------|-----------|------------|
| | | Pr | Re | F1 | IoU | Road420 | Facade390 | Concrete3k |
| adapter | ViT-B | 0.7574 | 0.7920 | 0.7610 | 0.6379 | 0.5859 | 0.4680 | 0.6573 |
| adapter | ViT-L | 0.7611 | 0.8004 | 0.7682 | 0.6464 | 0.6263 | 0.4700 | 0.6672 |
| adapter | ViT-H | 0.7676 | 0.7965 | 0.7704 | 0.6495 | 0.6149 | 0.4718 | 0.6718 |
| LoRA | ViT-B | 0.7512 | 0.7823 | 0.7523 | 0.6286 | 0.5905 | 0.4787 | 0.6557 |
| LoRA | ViT-L | 0.7623 | 0.7849 | 0.7608 | 0.6379 | 0.6162 | 0.4862 | 0.6791 |
| LoRA | ViT-H | 0.7620 | 0.7918 | 0.7639 | 0.6416 | 0.6222 | 0.4544 | 0.6798 |

6. Comparison with SOTA models

Semantic segmentation models typically consist of three main components: the backbone, neck, and head. The backbone plays a crucial role in extracting high-level and semantically rich features. The neck assists in fusing information across multiple scales, while the head can be viewed as a decoder, obtaining the desired mask through aggregation, upsampling, and refinement.

Twelve other models that have performed well in semantic segmentation are selected for comparative experiments with CrackSAM. These include VGG-UNet [46], Swin-UPerNet [25], MobileNet [60], UNet-FCN and UNet-PSPNet [17], ResNet-DeepLabV3+ [58], ViT-UPerNet [24], SegFormer [26], HRNet-FCN [61], and ResNet-PSPNet [62]. To ensure a fair comparison, the selected comparative models have significant differences in terms of parameter quantity and include various types of image backbones, such as CNN-based UNet, ResNet-50, and ResNet-101, and attention-based architectures such as Swin-T, ViT-B, and Mix Transformer (MiT-B5). One reason for choosing these models is their outstanding performance in prior crack segmentation tasks [27][28][53][63].

The architectures for comparative models are configured using the settings from the OpenMMLab segmentation toolkit [64]. The main training configuration is closely aligned with the CrackSAM. The maximum number of iterations is set to 200 epochs, and the initial learning rate is determined through multiple trial and error adjustments. Based on transfer learning, the parameters are initialized using the weights of baseline models that are pretrained on large datasets such as Cityscapes [65].

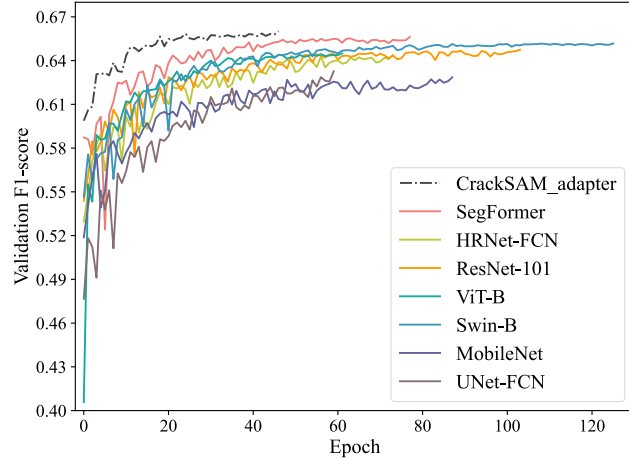


Figure 10 Changes in the F1-scores of different models on the validation set with training epochs. The batch size is set to 8. (For interpretation of the references to colour in this figure legend, the reader is referred to the web version of this article.)

As Figure 10 shows, fine-tuning a vision foundation model using PEFT requires fewer iterations to achieve convergence than training an entire relatively small model. Consequently, the total training duration does not significantly increase.

This study evaluates the performance of CrackSAM from two perspectives: robustness and generalization.

6.1 Evaluation on datasets with artificial noise

Artificial noise is introduced into the test set to assess the model robustness. This paper primarily investigates the following two cases when introducing artificial noise:

Case 1: For the input image I , reduce its brightness and apply Gaussian blur:

$$I' = (I - bri) * K \quad (13)$$

Bri represents the brightness, $*$ denotes the convolution operation, and K represents the Gaussian kernel. Specifically, the JPG image is converted to the HSV colour space. Then, 50 is subtracted from the V channel to achieve a decrease in brightness. Next, a 2D Gaussian filter with a kernel size of 9x9 is used to smooth the JPG image.

Case 2: Apply serious blur to the input image, followed by downsampling:

$$I' = (I * K) \downarrow_s \quad (14)$$

\downarrow denotes the downsampling operation, and S is the scaling factor. Gaussian blur is applied to the image with a kernel size of 21x21, after which the image is downsampled to half its original size via cubic interpolation, followed by interpolation back to the original size.

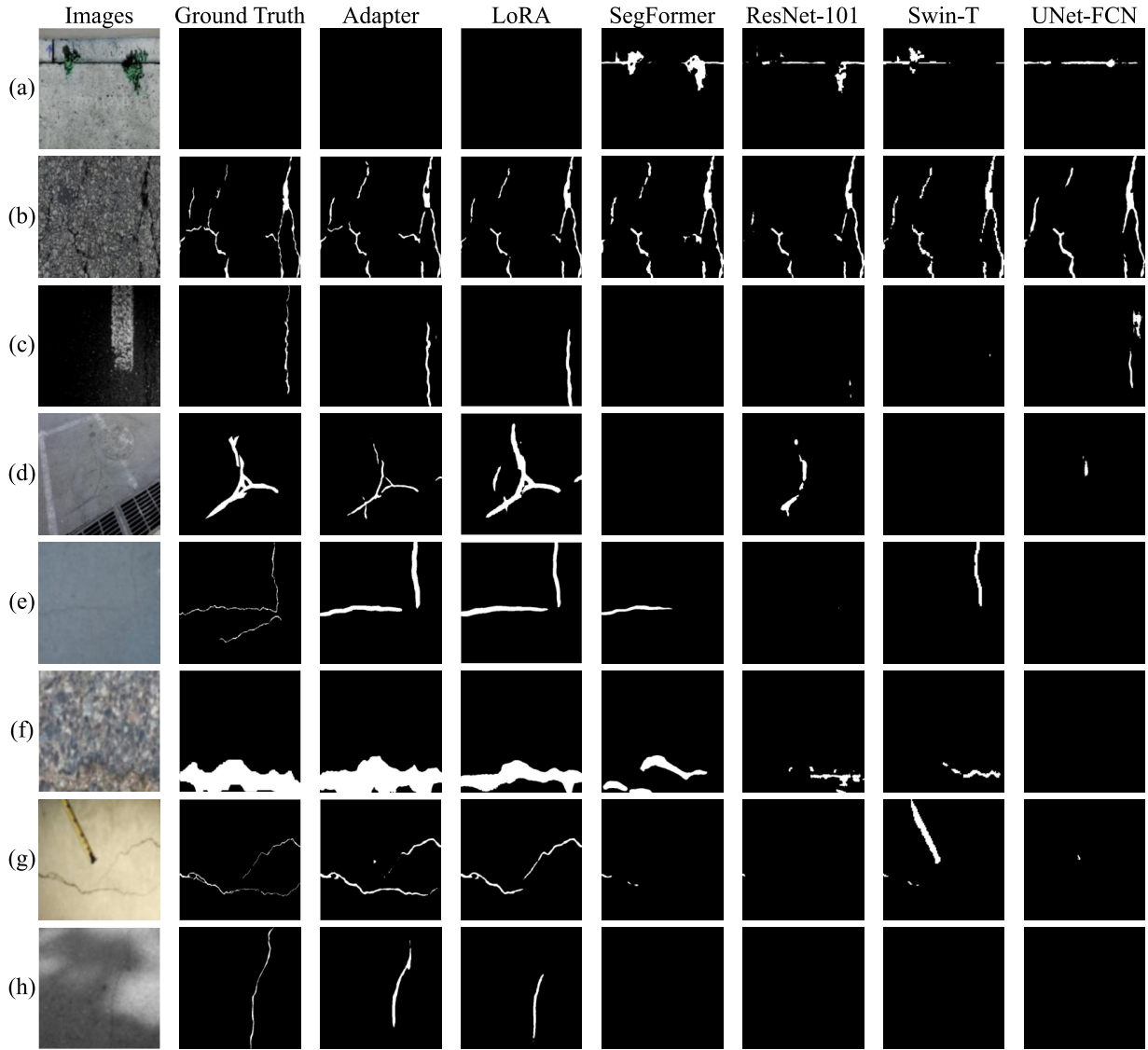


Figure 11 Inference results of comparative experiments on the test set with artificial noise.

The experimental results are listed in [Table 7](#), and some predicted masks are shown in [Figure 11](#).

[Figure 11](#) (a)-(d) are from case 1, simulating a dim environment. The remaining figures are from case 2, indicating a fuzzy situation. As the figure shows, the proposed CrackSAM performs well in identifying various forms of cracks, such as linear ([Figure 11](#) (c)), branched ([Figure 11](#) (d)), and webbed ([Figure 11](#) (b)). It is capable of predicting different materials (asphalt, concrete), various structures (road surfaces, walls, etc.), and diverse crack thicknesses, brightness levels, and contrast ratios.

[Figure 11](#) (a) is a noncrack image. Neither CrackSAM_adapter nor CrackSAM_LoRA provides any masks, while the other four comparative models identify construction joints and paint as cracks. This indicates that the crack classification task can be part of the crack segmentation task, eliminating the need for a two-stage design. When the model does not return any crack masks, the image is considered a noncrack image.

For extremely dark conditions (Figure 11 (c)), the CrackSAM can still identify some cracks, although a few may be indistinguishable from the background. In extremely blurry situations (Figure 11 (d), (e), (h)), CrackSAM can find most cracks that are difficult for the naked eye to discern, while other models can hardly detect the cracks present in the image.

Figure 12 studied the IoU of different models with different Gaussian kernel sizes when adding a Gaussian blur to images in the test set. As shown in the figure, CrackSAM demonstrates much greater robustness than do the other models. Despite the comparable performances of the compared models on the unprocessed test set, their IoUs significantly decrease when a Gaussian blur is added. When the Gaussian kernel size is 25, the performance of CrackSAM even surpasses that of ViT-B and Swin-B with a kernel size of 15.

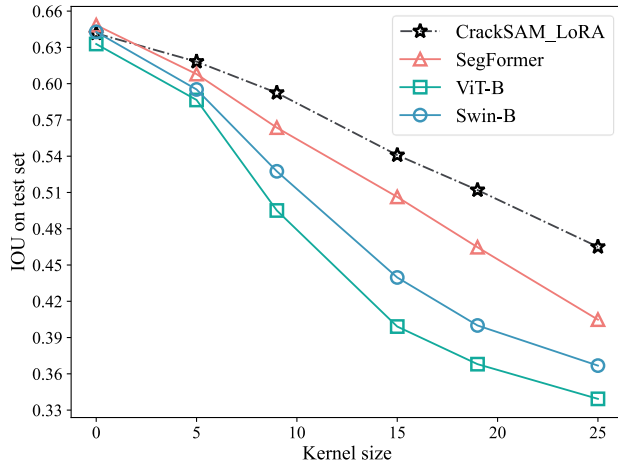


Figure 12 Variation in the IoU for different models under different Gaussian kernel sizes.

Table 7 reveals that almost all the models achieved satisfactory results on the original test set ($\text{IoU} \geq 0.62$), except for UNet-PSPNet, which performed relatively worse. Excluding UNet-PSPNet, the maximum gap between CrackSAM and the other 11 SOTA models is 4.6% on the original test set. However, significant differences emerge on the noisy test set, with variations reaching 27.0% and 42.0% in two specific cases. The classic UNet architecture performs poorly on severely blurred test sets, with UNet-FCN and UNet-PSPNet experiencing accuracy drops of 54.4% and 60.3%, respectively, after adding severe blur, while CrackSAM_LoRA experiences only a 23.4% drop. Among all the models, CrackSAM_adapter is the most accurate model on the test set, while CrackSAM_LoRA is the most accurate on the noisy test set. This shows that the robustness of the CrackSAM is much better than that of traditional models.

6.2 Zero-shot performance on unseen datasets

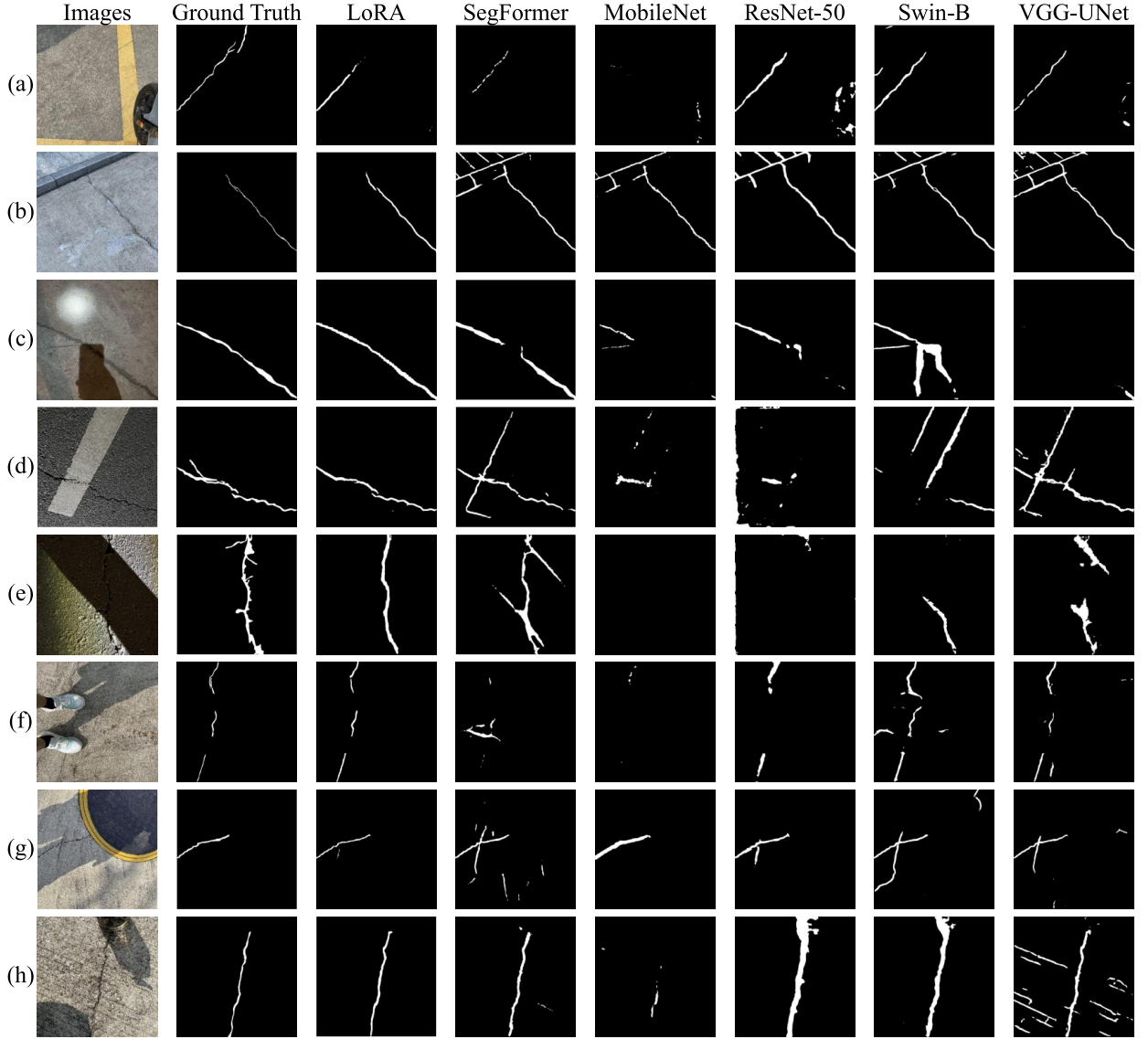


Figure 13 Zero-shot results of comparative experiments on Road420.

As Figure 13 shows, the proposed model yields satisfactory predictions at various scales and in various environments and under different interference conditions. In Figure 13 (a), cracks captured from a distant view become challenging to discern by the naked eye after downsampling, yet the AI models used in this experiment can still identify cracks in the image. This effectively highlights the superiority of deep learning algorithms in crack segmentation. For cracks captured at night, as Figure 13 (c), (d), and (e) show, CrackSAM maintains highly accurate predictions, particularly in Figure 13 (e), where the cracks almost merge with shadows, while CrackSAM still accurately identifies the cracks. However, other models are strongly affected by shadows and road markings, which can result in numerous artifacts. In Figure 13 (b), the CrackSAM correctly distinguishes between construction joints and cracks, but other models are misled by the sidewalk in the image. In Figure 13 (f), CrackSAM is not affected by occlusion and accurately outputs three segments of cracks, whereas

other models either produce artifacts or fail to recognize the three complete segments. CrackSAM correctly segments the cracks in [Figure 13](#) (g) with little influence from tire tracks on the road surface. In [Figure 13](#) (h), the segmentation performance of the CrackSAM remains unaffected by the presence of a cup and refracted light.

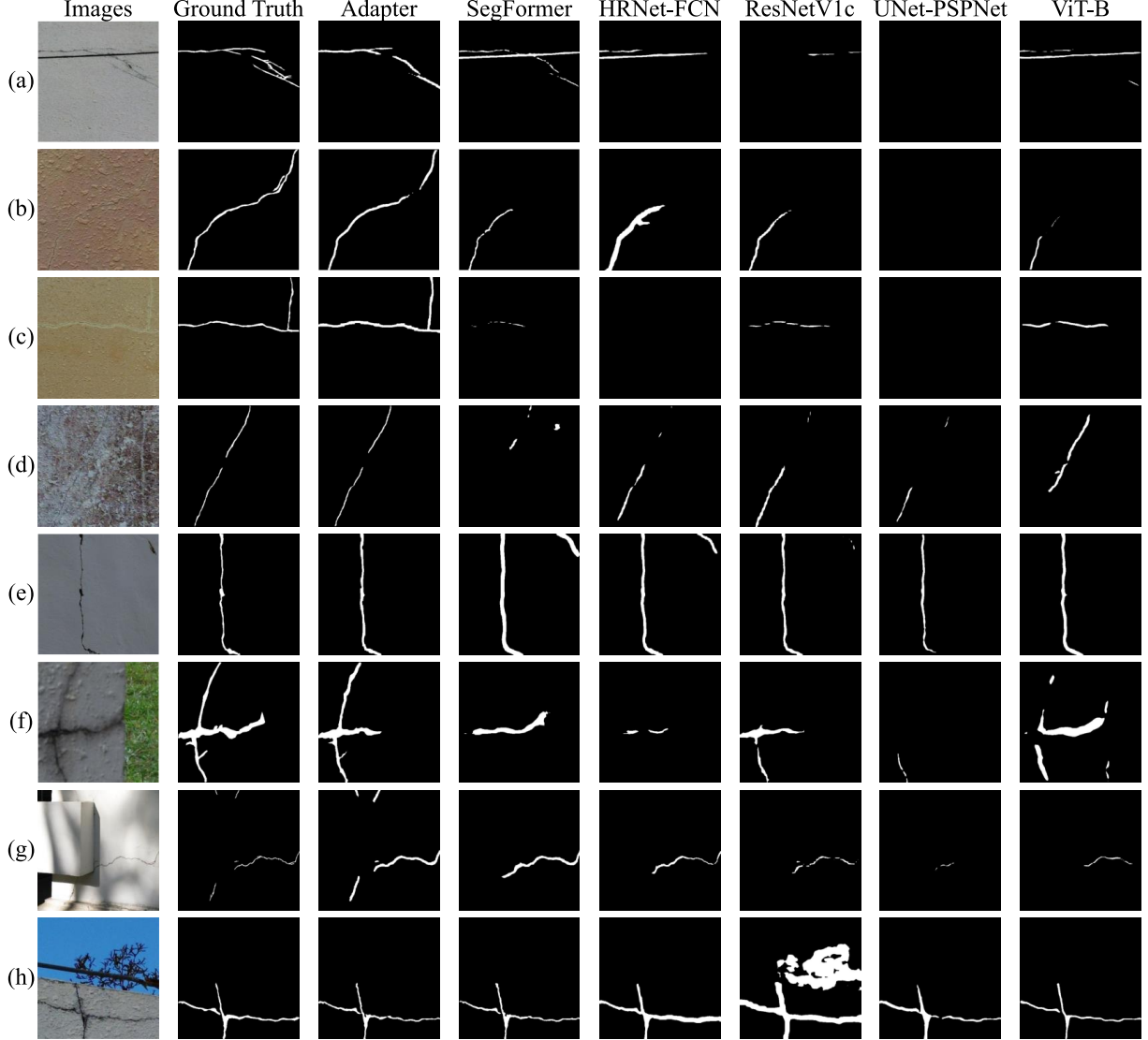


Figure 14 Zero-shot results of comparative experiments on Facade390.

Due to the impact of annotation thickness on the IoU of the model during the zero-shot operation on Facade390, which generally results in a lower IoU, it is necessary to combine the figures of the segmentation results when conducting comparative analysis on this dataset. As depicted in [Figure 14](#), the proposed model can effectively identify cracks in an automated and efficient manner when combined with UAVs, even when images are captured from different angles and distances. In [Figure 14](#) (a), other models struggle to distinguish between construction joints and cracks, whereas CrackSAM can. [Figure 14](#) (b) and (c) showcase red building facades with peeling, where the CrackSAM successfully segments small cracks, while the other models fail to do so. [Figure 14](#) (d) shows walls with paint and peeling, where due to severe interference, comparative models cannot

segment complete cracks, whereas CrackSAM provides results closest to the ground truth. [Figure 14](#) (f) shows surface cracks on the column with damp stains and grass; the segmentation mask of CrackSAM closely resembles the actual crack morphology. In [Figure 14](#) (g), at the junction of the beam and column with tree shadows, the CrackSAM identifies all four cracks, including the two small cracks at the top of the image.

According to [Table 7](#), similar to robustness, the generalization gap among different models is also substantial, reaching 42.9%, 33.0%, and 31.1% on three new datasets. Lightweight networks such as MobileNet-V3 and HRNet-FCN exhibit decent zero-shot performance on Concrete3k but perform poorly on the interference-filled Road420 dataset, demonstrating the limited feature extraction capability of small models. Several larger models, such as ViT-B and Swin-B, perform like CrackSAM on the test set, with acceptable performance on Road420; however, their prediction accuracy is sensitive to noise. The widely used ResNet model demonstrates reasonable robustness, but its performance on the Road420 dataset is unexpectedly poor. Both fine-tuned versions of CrackSAM exhibit excellent cross-dataset generalization capabilities. CrackSAM_LoRA is the best-performing model during the zero-shot operation on the Road420 and Concrete3k datasets, while CrackSAM_adapter performs better on Facade390. Among the twelve SOTA models, SegFormer is the best in terms of both robustness and generalizability. However, the proposed CrackSAM achieves a significant improvement in IoU metrics compared to SegFormer on the two noisy test sets and three new datasets, with increases of up to 11.1%, 10.8%, 7.0%, 2.1%, and 4.1%, indicating a notable improvement in performance.

[Table 7](#) also illustrates the significance of studying the robustness and generalizability of crack segmentation models, as they truly impact the feasibility of models for real-world applications. In summary, through comparative experiments, the proposed CrackSAM achieved the best results in terms of test set accuracy, robustness, and zero-shot performance.

The robust generalization ability of the CrackSAM is primarily attributed to the power of the large backbone and the effectiveness of the PEFT method. This is evident from comparative and ablation experiments, as CrackSAM does not perform as well when ViT-H and PEFT are not utilized.

Table 7 Comparison of the noisy dataset and unseen dataset with other SOTA models

| Model | Backbone | Parameters | Test set | Noisy test set 1 | Noisy test set 2 | Road420 | Facade390 | Concrete3k |
|-------------------------------------|---------------|----------------------------|---------------|-----------------------|----------------------------------|---------------|---------------|---------------|
| | | | - | -50 bri* + blur(k*=9) | $\times 1/2 + \text{blur}(k=21)$ | Zero-shot | Zero-shot | Zero-shot |
| CrackSAM_adapter (dim=32, s=0.2) | ViT-H | 641.9 M (Tunable 9.1 M) | 0.6495 | 0.5466 | 0.4763 | 0.6149 | 0.4718 | 0.6718 |
| CrackSAM_LoRA (qv, rank=4) | ViT-H | 637.2 M (Tunable 4.4 M) | 0.6416 | 0.5782 | 0.4915 | 0.6222 | 0.4544 | 0.6798 |
| VGG-UNet | VGG16 | 53.91 M | 0.6419 | 0.4337 | 0.3472 | 0.5126 | 0.4547 | 0.5152 |
| Swin-UPerNet | Swin-T | 58.9 M | 0.6199 | 0.4745 | 0.3963 | 0.4628 | 0.4065 | 0.4778 |
| Swin-UPerNet | Swin-B | 120.0 M | 0.6428 | 0.5003 | 0.3857 | 0.5262 | 0.4593 | 0.5655 |
| MobileNet-V3 | MobileNet-V3 | 3.28 M | 0.6208 | 0.5068 | 0.3738 | 0.4447 | 0.4322 | 0.6154 |
| UNet-FCN | UNet | 28.99 M | 0.6255 | 0.4218 | 0.2852 | 0.4531 | 0.3677 | 0.4682 |
| UNet-PSPNet | UNet | 28.97 M | 0.5594 | 0.3535 | 0.2222 | 0.3555 | 0.3163 | 0.5262 |
| ResNet-DeepLabV3+ | ResNet-101 | 60.2 M | 0.6402 | 0.5115 | 0.4088 | 0.3827 | 0.4399 | 0.5791 |
| ResNet-DeepLabV3+ | ResNet-50 | 41.2 M | 0.6395 | 0.5077 | 0.3947 | 0.3918 | 0.4402 | 0.5601 |
| ResNet-PSPNet | ResNetV1c-101 | 65.59 M | 0.6346 | 0.5110 | 0.4207 | 0.4084 | 0.4327 | 0.5544 |
| ViT-UPerNet | ViT-B | 142.1 M | 0.6328 | 0.4714 | 0.3554 | 0.5171 | 0.4276 | 0.6027 |
| SegFormer | MiT-B5 | 82.0 M | 0.6484 | 0.5204 | 0.4436 | 0.5817 | 0.4622 | 0.6533 |
| HRNet-FCN | HRNet-W18 | 9.63 M | 0.6356 | 0.5055 | 0.4434 | 0.4172 | 0.4214 | 0.6322 |

Note: *¹bri= brightness; *²k= kernel size.

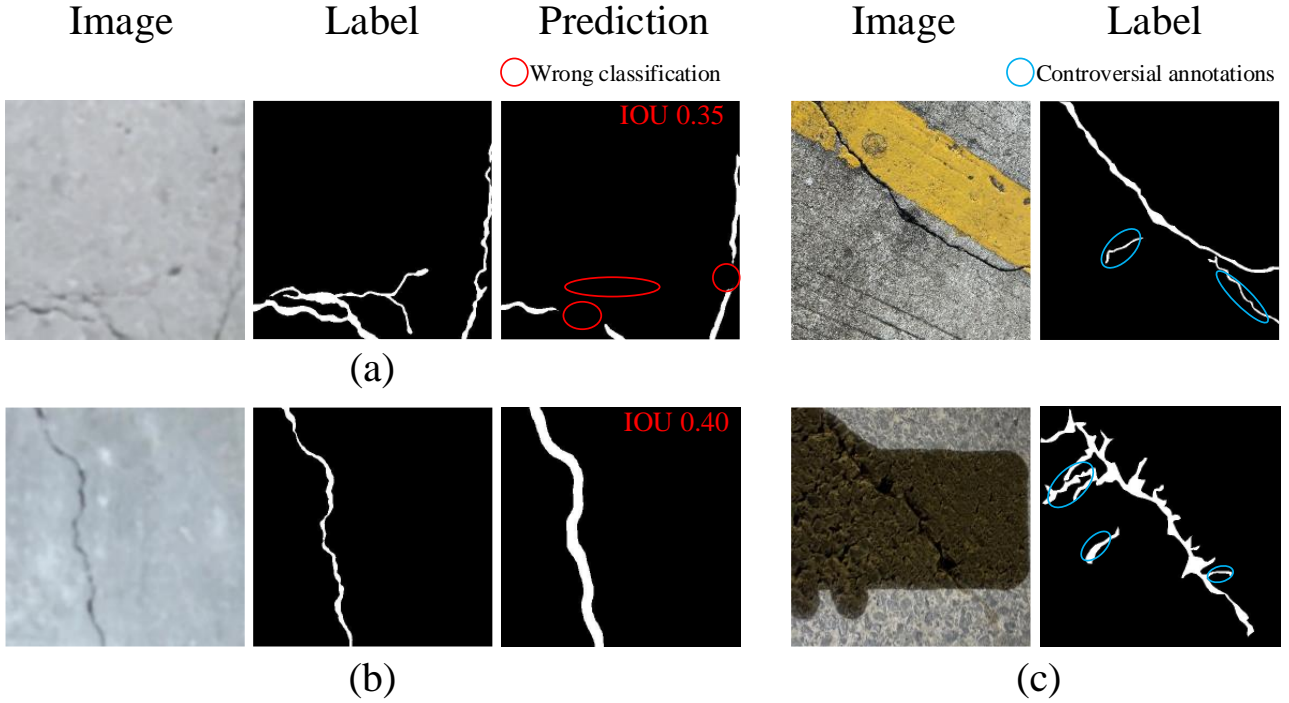


Figure 15 Several prediction situations with low IoUs. (a) Wrong classification. (b) Thicker prediction mask. (c) Controversial annotations subject to subjective judgements.

The issues affecting the model's accuracy can generally be categorized into three situations. In the first scenario, the model fails to recognize the semantics of a particular object, as illustrated in Figure 15 (a). This reflects a deficiency in the model. The second situation arises when the model correctly identifies a crack and successfully outputs its mask. However, because the output mask is much coarser than the annotation mask, the IoU is lower, while the recall is very high, as depicted in Figure 15 (b). This situation does not impact the normal recognition of cracks and is considered acceptable. In the third type, annotators, when providing high-quality annotations on high-resolution images, may label not only the main crack but also adjacent minor cracks and defects. Whether these tiny defects should be annotated depends on the annotator's subjective judgement (Figure 15 (c)). After downsampling, information about these minor defects is severely lost, rendering them unidentifiable. This situation often occurs in the annotation of asphalt road cracks, where asphalt and cracks have similar brightness and contrast ratios, leading to ambiguous situations.

7. Conclusions

This paper fine-tuned the segment anything model using PEFT methods for crack segmentation. The proposed CrackSAM was pretrained on more than 11k images. Two new labelled datasets comprising 810 images were collected through smartphones and UAVs for zero-shot. The main conclusions of this paper are as follows:

- (1) PEFT technology was utilized, with the image encoder of SAM frozen and a trainable delta

(adapter and LoRA) introduced on the ViT backbone. Fine-tuning was applied to the head and delta. The pretrained vision foundation model can be effectively introduced into crack segmentation.

(2) The proposed CrackSAM based on PEFT improved the IoU score greatly compared to the traditional method of fine-tuning only the head. The fine-tuning of the CrackSAM followed the scaling law, where using ViT-H as the backbone instead of ViT-B resulted in additional performance gains. The combination of the ViT-H backbone and the PEFT method is the main reason for the successful performance of the CrackSAM.

(3) Excessive over-parameterization can possibly enhance the performance on the test set but may not necessarily generalize to other datasets. Increasing the middle dimension of the adapter, raising the rank of the LoRA, and applying the LoRA to more positions often accompanied an increase in computational cost and a simultaneous decrease in generalization. Therefore, the fine-tuning design entails a tradeoff between complexity, performance, and generalization.

(4) CrackSAM worked exceptionally well in cross-scale and cross-scenario situations, exhibiting strong robustness and generalizability. In the evaluation of two artificially introduced noise scenarios and three previously unseen datasets, CrackSAM demonstrated a great improvement in IoU compared to the twelve SOTA models, ranging from 11.1% - 63.6%, 10.8% - 121.2%, 7.0% - 75.0%, 2.1% - 49.2%, and 4.1% - 45.2%, respectively.

(5) Satisfactory results were achieved on the test set by almost all the models, but there was a significant difference in generalizability. In complex environments with severe interference, noticeable advantages were demonstrated by CrackSAM. Considering the various factors that may affect crack segmentation in real-world deployment, it is essential to study the robustness and zero-shot capabilities of a newly proposed architecture.

The lack of large benchmark datasets in crack segmentation constrains the performance of AI models and their practical applications. The authors call for more open-source efforts and the establishment of a large-scale crack segmentation dataset with a unified standard.

If deploying a lighter network is necessary, it is recommended to employ knowledge distillation to train a lightweight model with guidance from CrackSAM. Furthermore, other powerful visual foundation models, such as the self-supervised DINOv2 [33], can be leveraged to detect cracks. This technique can also be extended to segment other types of structural defects, which enables the achievement of "segment everything" in SHM. These issues will be the focus of future work.

8. Declarations

8.1. Funding

The authors gratefully acknowledge the financial support provided by the National Natural Science Foundation of China, Grant No. 52308179.

8.2. Conflicts of interest

There are no conflicts of interest for this paper.

8.3. Data availability

All the utilized models, pretrained weights, and the labelled datasets will be publicly available on <https://github.com/KG-TSI-Civil/CrackSAM> after acceptance.

References

- [1] Zawad, Md Rahat Shahriar, et al. "A comparative review of image processing based crack detection techniques on civil engineering structures." *Journal of Soft Computing in Civil Engineering* 5.3 (2021): 58-74.
- [2] Wan, Kai Tai, and Christopher KY Leung. "Applications of a distributed fiber optic crack sensor for concrete structures." *Sensors and actuators A: physical* 135.2 (2007): 458-464.
- [3] Aggelis, D. G., et al. "Combined use of thermography and ultrasound for the characterization of subsurface cracks in concrete." *Construction and Building Materials* 24.10 (2010): 1888-1897.
- [4] Tashan, Jawdat, and R. Al-Mahaidi. "Detection of cracks in concrete strengthened with CFRP systems using infra-red thermography." *Composites Part B: Engineering* 64 (2014): 116-125.
- [5] Azimi, Mohsen, Armin Dadras Eslamlou, and Gokhan Pekcan. "Data-driven structural health monitoring and damage detection through deep learning: State-of-the-art review." *Sensors* 20.10 (2020): 2778.
- [6] Wang, Long, and Zijun Zhang. "Automatic detection of wind turbine blade surface cracks based on UAV-taken images." *IEEE Transactions on Industrial Electronics* 64.9 (2017): 7293-7303.
- [7] Liu, Yu - Fei, et al. "Image - based crack assessment of bridge piers using unmanned aerial vehicles and three - dimensional scene reconstruction." *Computer - Aided Civil and Infrastructure Engineering* 35.5 (2020): 511-529.
- [8] Gopalakrishnan, Kasthurirangan, et al. "Crack damage detection in unmanned aerial vehicle images of civil infrastructure using pre-trained deep learning model." *Int. J. Traffic Transp. Eng* 8.1 (2018): 1-14.
- [9] Sinha, Sunil K., and Paul W. Fieguth. "Automated detection of cracks in buried concrete pipe images." *Automation in construction* 15.1 (2006): 58-72.
- [10] Subirats, Peggy, et al. "Automation of pavement surface crack detection using the continuous wavelet transform." *2006 International Conference on Image Processing*. IEEE, 2006.
- [11] Zhang, Lei, et al. "Road crack detection using deep convolutional neural network." *2016 IEEE international conference on image processing (ICIP)*. IEEE, 2016.
- [12] Vaswani, Ashish, et al. "Attention is all you need." *Advances in neural information processing systems* 30 (2017).
- [13] Chen, Junjie, Weisheng Lu, and Jinfeng Lou. "Automatic concrete defect detection and reconstruction by aligning aerial images onto semantic - rich building information model." *Computer - Aided Civil and Infrastructure Engineering* 38.8 (2023): 1079-1098.
- [14] Kondo, Yuki, and Norimichi Ukita. "Joint Learning of Blind Super-Resolution and Crack Segmentation for Realistic Degraded Images." *arXiv preprint arXiv:2302.12491* (2023).
- [15] Houlsby, Neil, et al. "Parameter-efficient transfer learning for NLP." *International Conference on Machine Learning*. PMLR, 2019.
- [16] Hu, Edward J., et al. "Lora: Low-rank adaptation of large language models." *arXiv preprint arXiv:2106.09685* (2021).
- [17] Ronneberger, Olaf, Philipp Fischer, and Thomas Brox. "U-net: Convolutional networks for biomedical image segmentation." *Medical Image Computing and Computer-Assisted Intervention–MICCAI 2015: 18th International Conference, Munich, Germany, October 5-9, 2015, Proceedings, Part III* 18. Springer International Publishing, 2015.
- [18] Lin, Tsung-Yi, et al. "Feature pyramid networks for object detection." *Proceedings of the IEEE conference on computer vision and pattern recognition*. 2017.
- [19] Zhao, Hengshuang, et al. "Pyramid scene parsing network." *Proceedings of the IEEE conference on computer vision and pattern recognition*. 2017.
- [20] Chen, Liang-Chieh, et al. "Encoder-decoder with atrous separable convolution for semantic image

segmentation." Proceedings of the European conference on computer vision (ECCV). 2018.

[21] Zhang, Lingxin, Junkai Shen, and Baijie Zhu. "A research on an improved Unet-based concrete crack detection algorithm." Structural Health Monitoring 20.4 (2021): 1864-1879.

[22] Ren, Yupeng, et al. "Image-based concrete crack detection in tunnels using deep fully convolutional networks." Construction and Building Materials 234 (2020): 117367.

[23] Dais, Dimitris, et al. "Automatic crack classification and segmentation on masonry surfaces using convolutional neural networks and transfer learning." Automation in Construction 125 (2021): 103606.

[24] Dosovitskiy, Alexey, et al. "An image is worth 16x16 words: Transformers for image recognition at scale." arXiv preprint arXiv:2010.11929 (2020).

[25] Liu, Ze, et al. "Swin transformer: Hierarchical vision transformer using shifted windows." Proceedings of the IEEE/CVF international conference on computer vision. 2021.

[26] Xie, Enze, et al. "SegFormer: Simple and efficient design for semantic segmentation with transformers." Advances in Neural Information Processing Systems 34 (2021): 12077-12090.

[27] Shamsabadi, Elyas Asadi, et al. "Vision transformer-based autonomous crack detection on asphalt and concrete surfaces." Automation in Construction 140 (2022): 104316.

[28] Guo, Feng, et al. "Pavement crack detection based on transformer network." Automation in Construction 145 (2023): 104646.

[29] Bommasani, Rishi, et al. "On the opportunities and risks of foundation models." arXiv preprint arXiv:2108.07258 (2021).

[30] Kirillov, Alexander, et al. "Segment anything." arXiv preprint arXiv:2304.02643 (2023).

[31] Wang, Xinlong, et al. "Seggpt: Segmenting everything in context." arXiv preprint arXiv:2304.03284 (2023).

[32] Zou, Xueyan, et al. "Segment everything everywhere all at once." arXiv preprint arXiv:2304.06718 (2023).

[33] Oquab, Maxime, et al. "Dinov2: Learning robust visual features without supervision." arXiv preprint arXiv:2304.07193 (2023).

[34] Ahmadi, Mohsen, et al. "Application of segment anything model for civil infrastructure defect assessment." arXiv preprint arXiv:2304.12600 (2023).

[35] Zhou, Zhong, Junjie Zhang, and Chenjie Gong. "Hybrid semantic segmentation for tunnel lining cracks based on Swin Transformer and convolutional neural network." Computer - Aided Civil and Infrastructure Engineering (2023).

[36] Deng, Jia, et al. "Imagenet: A large-scale hierarchical image database." 2009 IEEE conference on computer vision and pattern recognition. Ieee, 2009.

[37] Lau, Stephen LH, et al. "Automated pavement crack segmentation using u-net-based convolutional neural network." Ieee Access 8 (2020): 114892-114899.

[38] Gao, Yuqing, et al. "Multiattribute multitask transformer framework for vision - based structural health monitoring." Computer - Aided Civil and Infrastructure Engineering (2023).

[39] Wang, Wei, et al. "A survey of zero-shot learning: Settings, methods, and applications." ACM Transactions on Intelligent Systems and Technology (TIST) 10.2 (2019): 1-37.

[40] Ding, Ning, et al. "Parameter-efficient fine-tuning of large-scale pre-trained language models." Nature Machine Intelligence 5.3 (2023): 220-235.

[41] Li, Xiang Lisa, and Percy Liang. "Prefix-tuning: Optimizing continuous prompts for generation." arXiv preprint arXiv:2101.00190 (2021).

[42] Lester, Brian, Rami Al-Rfou, and Noah Constant. "The power of scale for parameter-efficient prompt tuning." arXiv preprint arXiv:2104.08691 (2021).

[43] Chen, Tianrun, et al. "SAM Fails to Segment Anything?--SAM-Adapter: Adapting SAM in Underperformed Scenes: Camouflage, Shadow, and More." arXiv preprint arXiv:2304.09148 (2023).

[44] Wu, Junde, et al. "Medical sam adapter: Adapting segment anything model for medical image segmentation." arXiv preprint arXiv:2304.12620 (2023).

[45] Zhang, Kaidong, and Dong Liu. "Customized segment anything model for medical image segmentation." arXiv preprint arXiv:2304.13785 (2023).

[46] Khanhha, n.d. Khanhha/crack_segmentation. GitHub. URL https://github.com/khanhha/crack_segmentation#Dataset (accessed 11.9.23).

[47] Yang, Fan, et al. "Feature pyramid and hierarchical boosting network for pavement crack detection." IEEE Transactions on Intelligent Transportation Systems 21.4 (2019): 1525-1535.

[48] Eisenbach, Markus, et al. "How to get pavement distress detection ready for deep learning? A systematic approach." 2017 international joint conference on neural networks (IJCNN). IEEE, 2017.

- [49] Shi, Yong, et al. "Automatic road crack detection using random structured forests." *IEEE Transactions on Intelligent Transportation Systems* 17.12 (2016): 3434-3445.
- [50] Amhaz, Rabih, et al. "Automatic crack detection on two-dimensional pavement images: An algorithm based on minimal path selection." *IEEE Transactions on Intelligent Transportation Systems* 17.10 (2016): 2718-2729.
- [51] Zou, Qin, et al. "CrackTree: Automatic crack detection from pavement images." *Pattern Recognition Letters* 33.3 (2012): 227-238.
- [52] Liu, Yahui, et al. "DeepCrack: A deep hierarchical feature learning architecture for crack segmentation." *Neurocomputing* 338 (2019): 139-153.
- [53] Li, Yongshang, et al. "Real-time high-resolution neural network with semantic guidance for crack segmentation." *Automation in Construction* 156 (2023): 105112.
- [54] Tabernik, Domen, Matic Šuc, and Danijel Skočaj. "Automated detection and segmentation of cracks in concrete surfaces using joined segmentation and classification deep neural network." *Construction and Building Materials* 408 (2023): 133582.
- [55] Wang, Wenjun, and Chao Su. "Automatic concrete crack segmentation model based on transformer." *Automation in Construction* 139 (2022): 104275.
- [56] Hendrycks, Dan, and Kevin Gimpel. "Gaussian error linear units (gelus)." arXiv preprint arXiv:1606.08415 (2016).
- [57] Ba, Jimmy Lei, Jamie Ryan Kiros, and Geoffrey E. Hinton. "Layer normalization." arXiv preprint arXiv:1607.06450 (2016).
- [58] He, Kaiming, et al. "Identity mappings in deep residual networks." *Computer Vision–ECCV 2016: 14th European Conference, Amsterdam, The Netherlands, October 11–14, 2016, Proceedings, Part IV* 14. Springer International Publishing, 2016.
- [59] He, Kaiming, et al. "Masked autoencoders are scalable vision learners." *Proceedings of the IEEE/CVF conference on computer vision and pattern recognition*. 2022.
- [60] Howard, Andrew, et al. "Searching for mobilenetv3." *Proceedings of the IEEE/CVF international conference on computer vision*. 2019.
- [61] Sun, Ke, et al. "Deep high-resolution representation learning for human pose estimation." *Proceedings of the IEEE/CVF conference on computer vision and pattern recognition*. 2019.
- [62] He, Tong, et al. "Bag of tricks for image classification with convolutional neural networks." *Proceedings of the IEEE/CVF conference on computer vision and pattern recognition*. 2019.
- [63] Kulkarni, Shreyas, et al. "CrackSeg9k: a collection and benchmark for crack segmentation datasets and frameworks." *European Conference on Computer Vision*. Cham: Springer Nature Switzerland, 2022.
- [64] Chen, Kai, et al. "MMDetection: Open mmlab detection toolbox and benchmark." arXiv preprint arXiv:1906.07155 (2019).
- [65] Cordts, Marius, et al. "The cityscapes dataset for semantic urban scene understanding." *Proceedings of the IEEE conference on computer vision and pattern recognition*. 2016.